AIAA JOURNAL
Vol. 31, No. 5, May 1993

Deforming Grid Variational Principle for Unsteady Small Disturbance Flows in Cascades

Kenneth C. Hall*
Duke University, Durham, North Carolina 27708

A variational method for computing unsteady subsonic flows in turbomachinery blade rows is presented. A variational principle that describes the harmonic small disturbance behavior of the full potential equations about a nonlinear mean flow is developed. Included in this variational principle is the effect of a deforming computational grid that conforms to the motion of vibrating airfoils. Bilinear isoparametric finite elements are used to discretize the variational principle, and the resulting discretized equations are solved efficiently using lower-upper decomposition. The use of a deforming computational grid dramatically improves the accuracy of the method since no error-producing extrapolation is required to apply the upwash boundary conditions or to evaluate the unsteady pressure on the airfoil surfaces. Results computed using this technique are compared with experimental data and other analytical and computational methods.

I. Introduction

SIGNIFICANT progress in predicting unsteady flows in turbomachinery blade rows due to flutter and wake interaction has been made in recent years. Nevertheless, the accuracy and efficiency of unsteady aerodynamic analyses have lagged behind their steady counterparts. The goal of the present investigation is to improve the accuracy and efficiency of unsteady small disturbance potential flow calculations to a level comparable to equivalent steady flow calculations.

A number of investigators have examined unsteady flows in turbomachinery using the linearized potential[1-3] and linearized Euler[4,5] techniques. In the linearized approach, the unsteadiness in the flow is assumed to be small compared with the mean flow. Hence, the flowfield may be formally decomposed into a mean or steady component plus a harmonically varying perturbation flow. The equations that describe the perturbation flowfield are found to be linear variable coefficient equations that have coefficients that depend on the mean flowfield and the frequency of the unsteady excitation. The linearized equations are discretized on a computational grid and then solved either directly or iteratively depending on the size of the resulting matrix equations. The linearized analyses typically require one to two orders of magnitude less computer time than conventional time-accurate, time-marching techniques yet still retain the essential physics of the problem.

Until recently, most of the linearized methods have linearized the flow equations on a computational grid fixed in the relative frame of the blade row. For the flutter problem, however, the airfoils vibrate passing through the boundary of the fixed grid. Because the computational grid is fixed in space, the airfoil boundary conditions are applied at the mean location of the airfoils rather than at the instantaneous location. Therefore, additional extrapolation terms must be added to the unsteady airfoil boundary conditions to transfer the boundary conditions from the instantaneous location of the airfoil to its mean position. Once the unsteady velocity potential has been computed, similar extrapolation terms are required to evaluate the unsteady pressure on the airfoil surface. These extrapolation terms contain mean flow velocity derivatives that are difficult to evaluate—especially near the leading and trailing edges of the airfoils—limiting the accuracy of these methods.

A natural way to eliminate the extrapolation terms in the airfoil boundary conditions is to use a computational grid that conforms to the motion of the airfoils. Whitehead[3] used a modified perturbation velocity potential formulation that can be viewed as equivalent to using a rigidly moving computational grid. Although elastically deforming grids (as opposed to rigidly moving grids) have been widely used in time-accurate time-marching Euler analyses,[6-9] deforming grids have only recently been used in linearized analyses. Hall and Clark[10,11] and Holmes and Chuang[12] used elastically deforming computational grids in their linearized Euler analyses of unsteady subsonic and transonic flows in cascades. Hall and Clark[10] have numerically demonstrated the improved accuracy afforded by a deforming computational grid.

In this paper, an extension of Bateman's variational principle[13] is developed that describes the small disturbance behavior of the full potential equation. Included in the variational principle is the effect of an elastically deforming computational grid. This variational principle is discretized using bilinear isoparametric finite elements; the resulting set of linear equations is solved using lower-upper (LU) decomposition to obtain the unknown perturbation velocity potential.

The present deformable grid technique has a number of advantages over previous linearized potential methods. First, the accuracy is improved by eliminating the need to extrapolate to apply the upwash boundary conditions and to evaluate the unsteady pressure at the airfoil surfaces. Second, the current approach may be used with airfoils with chordwise deformation. Third, the finite element description is relatively simple to implement and extremely flexible allowing the use of structured or unstructured grids and a variety of element types. Fourth, the application of the upwash boundary conditions is simplified since the natural boundary conditions resulting from the variational principle automatically impose the correct upwash.

II. Theoretical Approach

A. Flowfield Description

In the present analysis, the flow through a compressor or turbine blade row is assumed to be inviscid, isentropic, irrotational, and two dimensional. Furthermore, the fluid is assumed to be an ideal gas with constant specific heats. These assumptions limit the range of applicability of the present analysis to subsonic and low-transonic speed flows with thin attached boundary layers.

Presented as Paper 92-0665 at the AIAA 30th Aerospace Sciences Meeting, Reno, NV, Jan. 6-9, 1992; received Jan. 14, 1992; revision received Oct. 24, 1992; accepted for publication Nov. 30, 1992.

*Assistant Professor, Department of Mechanical Engineering and Materials Science. Member AIAA.

Because the flow is assumed to be irrotational, the velocity field may be represented by the gradient of a scalar velocity potential $\hat{\phi}$. The conservation of mass in differential form is then

$$\frac{\partial \hat{\rho}}{\partial t} + \nabla \cdot (\hat{\rho} \nabla \hat{\phi}) = 0 \tag{1}$$

where $\hat{\rho}$ is the static density. The static density and pressure in terms of the velocity potential are found from integration of the momentum equation to be

$$\hat{\rho} = \rho_T \left\{ 1 - \frac{\gamma - 1}{C_T^2} \left[\tfrac{1}{2}(\nabla \hat{\phi})^2 + \frac{\partial \hat{\phi}}{\partial t} \right] \right\}^{\frac{1}{\gamma - 1}} \tag{2}$$

$$\hat{p} = p_T \left\{ 1 - \frac{\gamma - 1}{C_T^2} \left[\tfrac{1}{2}(\nabla \hat{\phi})^2 + \frac{\partial \hat{\phi}}{\partial t} \right] \right\}^{\frac{\gamma}{\gamma - 1}} \tag{3}$$

where p_T and ρ_T are the total pressure and density, respectively, γ is the ratio of specific heats, and C_T is the total speed of sound. Substitution of Eq. (2) into the continuity equation, Eq. (1), results in the well-known full potential equation

$$\nabla^2 \hat{\phi} = \frac{1}{\hat{c}^2} \left[\frac{\partial^2 \hat{\phi}}{\partial t^2} + 2 \nabla \hat{\phi} \cdot \nabla \frac{\partial \hat{\phi}}{\partial t} + \tfrac{1}{2} \nabla \hat{\phi} \cdot \nabla (\nabla \hat{\phi})^2 \right] \tag{4}$$

where $\hat{c}$ is the local speed of sound.

To complete the specification of the problem, boundary conditions must be specified on the surface S bounding the solution domain D (see Fig. 1). On the airfoil surfaces, there can be no mass flux through the airfoil surface so that

$$\hat{\rho} \nabla \hat{\phi} \cdot \hat{n} = \hat{\rho} \frac{\partial \hat{r}}{\partial t} \cdot \hat{n} \tag{5}$$

where the surface of the airfoil at any time t is described by the position vector $\hat{r}$. The wake may be thought of as an impermeable surface so that Eq. (5) also applies on both sides of the wake. In addition, no pressure discontinuity can exist across the wake so that

$$[\![\hat{p}]\!] = 0 \tag{6}$$

where $[\![\hat{p}]\!]$ is the pressure jump across the wake. Finally, for cascade flows, boundary conditions are required at the upstream and downstream far-field boundaries and at the periodic boundaries. The details of these boundary conditions will depend on the particular problem being solved.

B. Nonlinear Full Potential Variational Principle

Consider an unsteady, inviscid, irrotational flow that is temporally periodic with period T. The conservation of mass, Eq. (1), is the Euler equation of an extension of Bateman's variational principle[13] that states that the pressure integrated over the domain D and over one period T is extremized. Consider the functional

$$\Pi = \frac{1}{T} \int_T \iint_D \hat{p} \, dx \, dy \, dt + \frac{1}{T} \int_T \oint_S \hat{Q} \hat{\phi} \, ds \, dt \tag{7}$$

where $\hat{Q}$ is the prescribed mass flux on the boundary and s is the distance along the boundary. Taking the first variation of Π gives

$$\delta \Pi = \frac{1}{T} \int_T \iint_D \delta \hat{p} \, dx \, dy \, dt + \frac{1}{T} \int_T \oint_S \hat{Q} \delta \hat{\phi} \, ds \, dt \tag{8}$$

where the variation of the pressure is

$$\delta \hat{p} = -\hat{\rho} \left(\nabla \hat{\phi} \cdot \nabla \delta \hat{\phi} + \frac{\partial}{\partial t} \delta \hat{\phi} \right)$$

The first integral in Eq. (8) contains derivatives of the variation in $\hat{\phi}$. To eliminate these derivatives, the divergence theorem is applied to the first term, whereas integration by parts is applied to the second term. The resulting expression for the variation in Π is given by

$$\delta \Pi = \frac{1}{T} \int_T \iint_D \left[\nabla \cdot (\hat{\rho} \nabla \hat{\phi}) + \frac{\partial \hat{\rho}}{\partial t} \right] \delta \hat{\phi} \, dx \, dy \, dt + \frac{1}{T} \int_T \oint_S \left(\hat{Q} - \hat{\rho} \frac{\partial \hat{\phi}}{\partial n} \right) \delta \hat{\phi} \, ds \, dt \tag{9}$$

For Π to be stationary, $\delta \Pi$ must be zero for all admissible variations in $\hat{\phi}$. In the domain D, therefore, the conservation of mass must be satisfied. On the boundary S, two possibilities exist. On regions of the boundary where Dirichlet boundary conditions are imposed, the variation in $\hat{\phi}$ is zero and the integrand vanishes. On regions of the boundary where $\hat{\phi}$ is not specified, the quantity multiplying $\delta \hat{\phi}$ in the surface integral integrand must vanish, resulting in the Neumann boundary condition $\hat{\rho} \partial \hat{\phi} / \partial n = \hat{Q}$.

This variational principle, with some modifications to account for the cascade periodicity, wake, and far-field boundaries, can be applied to cascade flows. In theory, the variational principle could be used to set up a nonlinear finite element description of the flow. Such a finite element description would be nonlinear and three dimensional, however, with time being the third dimension. Furthermore, one cannot time march such a finite element model since past times are related to future times through the temporal periodicity condition. The potential at all time levels and spatial locations would have to be solved for simultaneously, making the numerical solution extremely expensive.

To overcome the difficulty introduced by the temporal integration in the aforementioned variational principle, the temporal behavior of the potential will be represented by assumed mode shapes. The temporal integration in the functional Π may then be carried out, resulting in simplified functionals and variational principles for the spatial behavior of the flow.

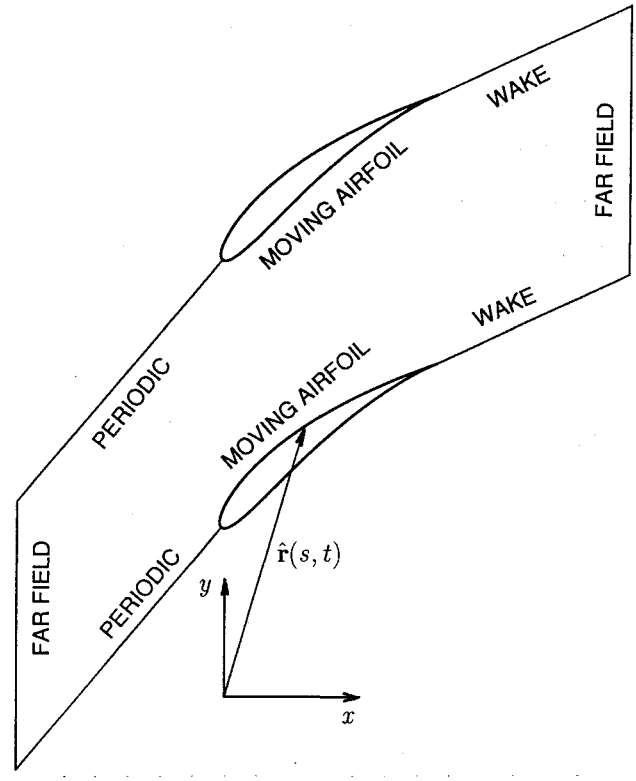

Fig. 1 Typical solution domain used for calculation of flow through cascades. Five main boundary types are moving airfoil, upstream periodic, downstream periodic/wake, upstream far field, and downstream far field.

The variational principles are then discretized using traditional finite element techniques.

C. Steady Flow Variational Principle

For steady flow, the resulting variational principle is particularly simple. The potential, pressure, and density are constant in time, i.e.,

$$\hat{\phi}(x, y, t) = \Phi(x, y) \tag{10a}$$

$$\hat{p}(x, y, t) = P(x, y) \tag{10b}$$

$$\hat{\rho}(x, y, t) = R(x, y) \tag{10c}$$

Substitution into the functional Π, Eq. (7), gives

$$\Pi_{\text{steady}} = \iint_D P \, dx \, dy + \oint_S Q\Phi \, ds \tag{11}$$

Taking the variation of Eq. (11) and setting the variation to zero give

$$\delta\Pi_{\text{steady}} = \iint_D \delta P \, dx \, dy + \oint_S Q\delta\Phi \, ds$$

$$= -\iint_D R \nabla\Phi \cdot \nabla\delta\Phi \, dx \, dy + \oint_S Q\delta\Phi \, ds = 0$$

which after application of the divergence theorem simplifies to

$$\delta\Pi_{\text{steady}} = \iint_D [\nabla \cdot (R \nabla\Phi)]\delta\Phi \, dx \, dy + \oint_S \left(Q - R\frac{\partial\Phi}{\partial n}\right)\delta\Phi \, ds = 0 \tag{12}$$

The Euler equation for this variational principle is clearly seen to be the steady conservation of mass. The natural boundary condition is the Neumann condition $R\partial\Phi/\partial n = Q$.

The steady variational principle, with minor modifications required for cascade flows, is used as the basis of a finite element technique for computing the steady flow. Because the Euler equation is nonlinear, one must resort to nonlinear finite element techniques. A Newton iteration technique is used to reduce the nonlinear problem to a series of linear problems, each of which is similar to the solution of the unsteady small disturbance flow to be described shortly. As the unsteady flow problem is the primary concern of this paper, the details of the nonlinear solution procedure will not be presented.

D. Small Disturbance Flow Variational Principles

Thus far, two variational principles have been presented, one for unsteady periodic flow and one for steady flow. Both variational principles resulted in nonlinear Euler equations. For many unsteady flows of interest, such as those that arise in the aeroelastic phenomena of flutter and forced response, the unsteadiness in the flow is relatively small compared with the mean flowfield. In such cases, the flow may be modeled as the sum of a nonlinear mean flow that is described by the steady nonliner potential equation [the Euler equation of Eq. (12)] and an unsteady perturbation flow that is described by a linearized small disturbance form of the full potential equation.[1-3] An extension to Bateman's variational principle is presently developed, which has as its Euler equation the linearized potential equations. Included in the variational principle is the effect of a deforming computational grid that conforms to the motion of vibrating airfoils.

In the present analysis, the computational grid is allowed to undergo small rigid body and elastic deformations. Shown in Fig. 2 is a typical computational grid as viewed in the physical coordinate system (x, y) and the computational or "strained" coordinate system (ξ, η). The physical coordinate system is related to the strained coordinate system by the perturbation series

$$x(\xi, \eta, \tau) = \xi + f(\xi, \eta, \tau) \tag{13a}$$

$$y(\xi, \eta, \tau) = \eta + g(\xi, \eta, \tau) \tag{13b}$$

$$t(\xi, \eta, \tau) = \tau \tag{13c}$$

The strained coordinates (ξ, η) are to zeroth-order equal to the physical coordinates (x, y). The first-order perturbation functions f and g describe the small perturbation motion of the physical grid about its mean position.

In a similar fashion, the unsteady potential is represented as the sum of a mean potential and a perturbation potential, both of which are functions of the strained coordinate system. Hence,

$$\hat{\phi}(\xi, \eta, \tau) = \Phi(\xi, \eta) + \phi(\xi, \eta, \tau) \tag{14a}$$

where the steady velocity potential Φ is known from the solution of the steady flow equations, and ϕ is the unknown unsteady perturbation potential. Note that, although Φ appears steady in the strained coordinate system (ξ, η), in the physical coordinate system (x, y), Φ is unsteady. Hence, the unsteadiness in the flow arises both from the motion of the

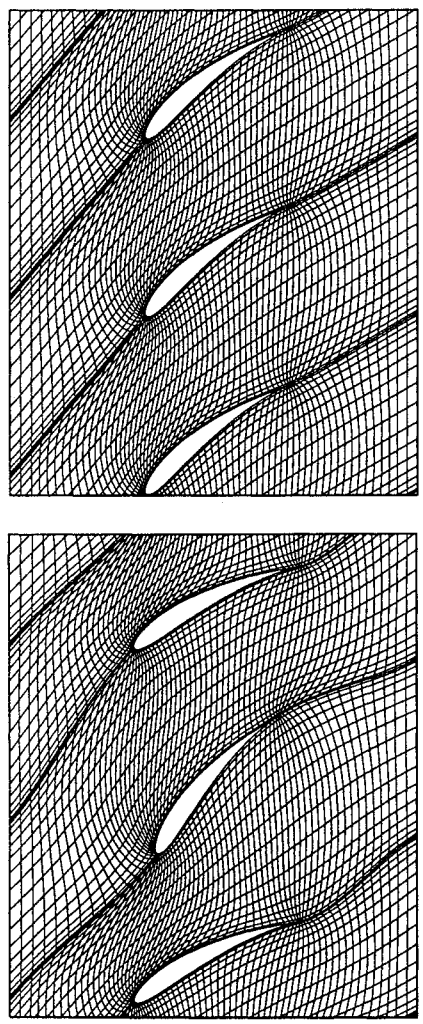

Fig. 2 Computational grid: a) in computational coordinate system (ξ, η); b) in physical coordinate system (x, y) for the case of a cascade of airfoils pitching about their midchords with an interblade phase angle σ of -180 deg.

grid and the perturbation potential ϕ. Similarly, the pressure and density are expanded in the perturbation series

$$\hat{p}(\xi, \eta, \tau) = P(\xi, \eta) + p(\xi, \eta, \tau) \tag{14b}$$

$$\hat{\rho}(\xi, \eta, \tau) = R(\xi, \eta) + \rho(\xi, \eta, \tau) \tag{14c}$$

This coordinate transformation and choice of perturbation series are similar to the method of strained coordinates that Lighthill[14] used to solve singular perturbation problems. Since the present problem is, strictly speaking, a regular perturbation problem for airfoils with finite radius leading edges, the proposed coordinate straining is not required to formulate the problem. Nevertheless, using a deforming grid eliminates the need to extrapolate to apply the airfoil boundary conditions or to compute the unsteady surface pressure, dramatically improving the accuracy of the method.

To first order, the operators ∇ and $\partial/\partial t$ can be expressed in terms of the strained coordinate system operators ∇' and $\partial/\partial\tau$ as follows:

$$\nabla = \begin{pmatrix} \frac{\partial}{\partial x} \\ \frac{\partial}{\partial y} \end{pmatrix} = \begin{bmatrix} 1 - f_\xi & -g_\xi \\ -f_\eta & 1 - g_\eta \end{bmatrix} \begin{pmatrix} \frac{\partial}{\partial \xi} \\ \frac{\partial}{\partial \eta} \end{pmatrix} = J\nabla' \tag{15a}$$

and

$$\frac{\partial}{\partial t} = \frac{\partial}{\partial \tau} - \frac{\partial f}{\partial \tau} \cdot \nabla' \tag{15b}$$

where f is the vector of grid motion functions $(f, g)^T$.

Having defined these differential operators, the unsteady pressure is expressed in the strained coordinate system by substituting Eqs. (15a) and (15b) into Eq. (3), resulting in the nonlinear Bernoulli's equation

$$\hat{p} = p_T \left\{ 1 - \frac{\gamma - 1}{C_T^2} \left[\tfrac{1}{2} \nabla' \hat{\phi}^T J^T J \nabla' \hat{\phi} + \frac{\partial \hat{\phi}}{\partial \tau} - f_\tau \cdot \nabla' \hat{\phi} \right] \right\}^{\frac{\gamma}{\gamma - 1}} \tag{16}$$

Expanding Eq. (16) in powers of ϕ, f, and g and collecting terms of first order give the perturbation pressure in terms of the steady and unsteady velocity potentials and the grid motion, i.e.,

$$p = -R \left[\nabla' \Phi^T \nabla' \phi + \frac{\partial \phi}{\partial \tau} - f_\tau \cdot \nabla' \Phi + \tfrac{1}{2} \nabla' \Phi^T \tilde{J} \nabla' \Phi \right] \tag{17}$$

where

$$\tilde{J} = J^T J - I = -\begin{bmatrix} 2f_\xi & (g_\xi + f_\eta) \\ (g_\xi + f_\eta) & 2g_\eta \end{bmatrix} + \Theta(f^2, f \cdot g, g^2)$$

The first and second terms on the right-hand side of Eq. (17) are the usual terms found in the linearized Bernoulli's equation for a coordinate system fixed in space. The third and fourth terms in Eq. (17) appear because the mean flowfield deforms with the grid. The third term on the right-hand side is due to the unsteady potential resulting from the translation of the mean velocity field. The fourth term is due to an unsteady velocity induced by local dilation and shearing of the mean potential field and does not contribute if the grid motion is rigid body [compare with Eq. (15) of Ref. 3].

Consider next the extension of Bateman's variational principle to a deforming volume D bounded by a moving surface S. Again, the variational principle is given by Eq. (7). However, because the domain D is deforming, the order of integration may not be interchanged if the physical coordinate system (x, y) is used. For this reason, it will be convenient to perform the integration in the strained coordinate system (ξ, η). In the strained coordinate system, the domain D does not deform with time and hence the order of integration may be interchanged. Neglecting for the moment the boundary integral term, the resulting functional is given by

$$\Pi_{\text{unsteady}} = \frac{1}{T} \int_T \iint_D \hat{p} |J^{-1}| \, d\xi \, d\eta \, d\tau \tag{18}$$

Since a linearized (small disturbance) version of the mass conservation statement is desired, the integrand of Eq. (18) is expanded about the mean solution in powers of ϕ, f, and g retaining up to quadratic terms. Terms of order ϕ^3, f^3, $\phi^2 f$, etc., and higher will contribute quadratic and higher order terms to the resulting Euler equation and hence may be ignored. Furthermore, the zeroth-order part of the Euler equation that results from first-order terms in the functional will be the same as the Euler equation for the steady flow and hence will be zero. After discarding terms that will not contribute to the first-order Euler equation, the functional to be made stationary is found to be

$$\begin{aligned} \Pi_{\text{linear}} = \frac{1}{T} \int_T \iint_D \frac{1}{2} R \Bigg[& -\nabla' \phi^T \nabla' \phi \\ & + \frac{1}{C^2} (\nabla' \Phi^T \nabla' \phi + \phi_\tau)^2 \Bigg] d\xi \, d\eta \, d\tau \\ & - \frac{1}{T} \int_T \iint_D R \Big\{ [\nabla' \Phi^T \tilde{J} \nabla' \phi \\ & + \nabla' \cdot f (\nabla' \Phi^T \nabla' \phi + \phi_\tau) - f_\tau \cdot \nabla' \phi] \\ & - \frac{1}{C^2} [(\tfrac{1}{2} \nabla' \Phi^T \tilde{J} \nabla' \Phi - f_\tau \cdot \nabla' \Phi) \\ & \times (\nabla' \Phi^T \nabla' \phi + \phi_\tau)] \Big\} \, d\xi \, d\eta \, d\tau \end{aligned} \tag{19}$$

Note that the first integral, which contains the second-order terms in ϕ, does not depend on the grid motion.

Next, after taking the variation of Π_{linear} and application of the divergence theorem and integration by parts, one finds that the resulting Euler equation is given by

$$\begin{aligned} & \nabla' \cdot R \nabla' \phi - \nabla' \cdot \left[\frac{R}{C^2} (\nabla' \Phi^T \nabla' \phi + \phi_\tau) \nabla' \Phi \right] \\ & - \frac{R}{C^2} (\nabla' \Phi^T \nabla' \phi_\tau + \phi_{\tau\tau}) \\ & = -\nabla' \cdot [R(\tilde{J} \nabla' \Phi + \nabla' \cdot f \nabla' \Phi)] + f_\tau \cdot \nabla' R \\ & + \nabla' \cdot \left[\frac{R}{C^2} (\tfrac{1}{2} \nabla' \Phi^T \tilde{J} \nabla' \Phi \nabla' \Phi - f_\tau \cdot \nabla' \Phi \nabla' \Phi) \right] \\ & + \frac{R}{C^2} [\tfrac{1}{2} \nabla' \Phi^T \tilde{J}_\tau \nabla' \Phi - f_{\tau\tau} \cdot \nabla' \Phi] \end{aligned} \tag{20}$$

Equation (20) is the desired linearized potential equation in the strained coordinate system. Note that the homogeneous part (the left-hand side) is independent of the grid motion. The inhomogeneous part (the right-hand side) is a function of the known steady flow and the prescribed grid motion.

The upwash boundary conditions on the airfoil surfaces are the natural boundary conditions that result from the variational principle and are given by

$$\frac{\partial \phi}{\partial n} = f_\tau \cdot \bar{n} - \tilde{J} \nabla \Phi \cdot \bar{n} \tag{21}$$

The first term on the right-hand side of Eq. (21) represents the upwash due to the local airfoil velocity normal to the surface. The second term on the right-hand side represents an addi-

tional upwash required to counter a downwash produced by shearing motion of the grid and hence shearing of the steady potential field in the vicinity of the airfoil surface. No upwash due to the local rotation of the airfoil appears in the natural boundary conditions, nor is it required. Since the mean potential field moves with the airfoil, the mean flow velocity vector is automatically aligned with the instantaneous position of the airfoil surface (at least for rigid body rotation of the grid).

To simplify matters further, it will be convenient to assume that the perturbation variables undergo simple harmonic motion. Most unsteady flows of interest to turbomachinery aeroelasticians are temporally periodic, e.g., flows due to blade flutter or wake/rotor interaction. Hence, the unsteady flow may be represented as a Fourier series in time. Since the governing small disturbance equations are linear, each Fourier mode may be analyzed individually, then summed together to form the complete solution. Therefore, without loss of generality, it is assumed that

$$\phi(\xi,\eta,\tau)\rightarrow \mathrm{Re}[\phi(\xi,\eta)e^{j\omega t}] = \tfrac{1}{2}[\phi(\xi,\eta)e^{j\omega t} + \bar{\phi}(\xi,\eta)e^{-j\omega t}] \quad (22)$$

where $\phi(\xi, \eta)$ is now the complex amplitude of the perturbation potential, and $\bar{\phi}(\xi, \eta)$ is its complex conjugate. Similar assumptions are made about all of the other perturbation quantities, including the grid motion functions.

Substitution of the harmonic motion assumption into the functional Π_{linear} yields the functional for the variational principle that describes the behavior of the harmonic small disturbance potential ϕ. Boundary integral terms are added to the functional at this point that will produce appropriate periodic boundary and wake boundary conditions. The result is

$$\begin{aligned}
\Pi_{\text{shm}} = \frac{1}{2}\int\int_D R\Big\{ & -\nabla'\bar{\phi}^T\nabla'\phi + \frac{1}{C^2}[\nabla'\bar{\phi}^T\nabla'\Phi\nabla'\Phi^T\nabla'\phi \\
& + j\omega(\nabla'\bar{\phi}^T\nabla'\Phi\phi - \bar{\phi}\nabla'\Phi^T\nabla'\phi) + \omega^2\bar{\phi}\phi]\Big\}\ d\xi\ d\eta \\
& - \int\int_D R\{\nabla'\Phi^T\tilde{J}\nabla'\bar{\phi} + \nabla'\cdot f(\nabla'\Phi^T\bar{\phi} - j\omega\bar{\phi}) \\
& - j\omega f\cdot\nabla'\bar{\phi} - \frac{1}{C^2}[(\tfrac{1}{2}\nabla'\Phi^T\tilde{J}\nabla'\Phi \\
& - j\omega f\cdot\nabla'\Phi)(\nabla'\Phi^T\nabla'\bar{\phi} - j\omega\bar{\phi})]\}\ d\xi\ d\eta \\
& + \int_{S_{\text{periodic}}} \lambda(\bar{\phi}_u e^{j\sigma} - \bar{\phi}_l)\ ds \\
& - \int_{S_{\text{wake}}} \left(V\frac{\partial r}{s} + j\omega r\right)(\bar{\phi}_u e^{j\sigma} - \bar{\phi}_l)\ ds \\
& + \text{complex conjugate terms} \qquad (23)
\end{aligned}$$

where the subscripts u and l denote the upper and lower surface of the wake, and V is the mean flow tangential velocity along the wake. A Lagrange multiplier λ is used in the third integral to enforce cascade periodicity on the upstream periodic boundary. The fourth integral in Eq. (23) is introduced to enforce flow tangency on the wake. The wake is modeled as an impermeable surface that oscillates harmonically with an unknown displacement r. An auxiliary equation that enforces pressure continuity across the wake provides closure for the wake displacement. Using this "wake fitting," the Kutta condition is automatically satisfied at the trailing edge of the airfoil.

Taking the variation of Eq. (23) and applying the divergence theorem results in the Euler equation and natural boundary conditions that describe the harmonic small disturbance behavior of the flow. The Euler equation, i.e., the linearized harmonic potential equation, is given by

$$\begin{aligned}
& \nabla'\cdot R\nabla'\phi - \nabla'\cdot\left[\frac{R}{C^2}(\nabla'\Phi^T\nabla'\phi + j\omega\phi)\nabla'\Phi\right] \\
& - \frac{R}{C^2}(j\omega\nabla'\Phi^T\nabla'\phi - \omega^2\phi) \\
& = -\nabla'\cdot[R(\tilde{J}\nabla'\Phi + \nabla'\cdot f\nabla'\Phi)] + j\omega f\cdot\nabla' R \\
& + \nabla'\cdot\left[\frac{R}{C^2}(\tfrac{1}{2}\nabla'\Phi^T\tilde{J}\nabla'\Phi\nabla'\Phi - j\omega f\cdot\nabla'\Phi\nabla'\Phi)\right] \\
& + \frac{R}{C^2}\left[\frac{j\omega}{2}\nabla'\Phi^T\tilde{J}\nabla'\Phi + \omega^2 f\cdot\nabla'\Phi\right] \qquad (24)
\end{aligned}$$

As expected, Eq. (24) is identical to Eq. (20) with the operator $\partial/\partial t$ replaced by $j\omega$.

The natural boundary conditions that result from this variational principle are as follows. On the airfoil surfaces, the natural boundary condition produces an upwash given by

$$\frac{\partial\phi}{\partial n} = j\omega f\cdot\bar{n} - \tilde{J}\nabla\Phi\cdot\bar{n} \qquad (25a)$$

This provides the correct upwash provided the grid motion conforms to the motion of the airfoil. Similarly, the boundary condition on the wake is

$$\frac{\partial\phi}{\partial n} = j\omega f\cdot\bar{n} - \tilde{J}\nabla\Phi\cdot\bar{n} + V\frac{\partial r}{\partial s} + j\omega r \qquad (25b)$$

Note the similarity of Eq. (25a) to Eq. (25b). The last two terms on the right-hand side of Eq. (25b) represent the additional upwash due to the wake displacement r.

Finally, on the periodic boundary, the natural boundary condition requires that traveling wave periodicity be satisfied, i.e.,

$$\phi(\xi,\ \eta + G) = \phi(\xi,\ \eta)e^{j\sigma} \qquad (25c)$$

where G is the blade-to-blade gap, and σ is the interblade phase angle. [Note that an Euler equation and natural boundary conditions also exist for $\bar{\phi}$ and are just the complex conjugates of Eqs. (24, 25a–25c).]

III. Numerical Solution Technique

Because the steady and unsteady solutions are spatially periodic, the solution domain can be reduced to a single blade passage. Within a passage, an H grid is generated using an algorithm based on the elliptic grid generation technique of Thompson et al.[15] A typical H grid for a cascade of compressor blades is shown in Fig. 2. Note that multiple passages are shown for clarity; only a single passage is used in actual computations.

The steady flowfield, which must be computed before the unsteady flow can be determined, is computed using a nonlinear finite element algorithm. A Newton iteration technique is used to reduced the nonlinear problem to a series of linear problems, each of which is similar to the finite element solution developed later for the linearized unsteady problem.[3,5] The Newton iteration technique is very efficient; typical problems require about five iterations to converge.

Having defined the steady grid and computed the steady flowfield, we now assume that this steady grid and steady flow solution define the mean grid position and mean flow solution. It still remains, however, to prescribe the grid motion perturbation functions f and g. The requirements on the grid motion are that the motion of the grid conform to the motion of the vibrating airfoils, that the motion should satisfy cascade periodicity along the upstream periodic and downstream wake boundaries, and that the motion of the grid go to zero in the

far field. The last requirement is made to simplify the implementation of the far-field boundary conditions. In addition, it is desirable from a computational standpoint to have a spatially smooth grid motion.

Because a smooth grid motion is desired, Laplace's equation is used to describe the behavior of the grid perturbation functions f and g on the interior of the grid. A finite element technique is used to discretize $\nabla'^2 f = 0$ and $\nabla'^2 g = 0$. Dirichlet boundary conditions, which satisfy the previous set of requirements for the grid motion, are specified on the boundary of the computational domain. The resulting discretized equations are solved directly using LU decomposition. The unsteady grid generation portion of the unsteady flow calculation requires about 10% of the total computational time.

A typical unsteady grid motion is depicted in Fig. 2. For this example, the blades are pitching about their midchords with an amplitude of 0.2 rad. Shown are the x and y locations of the grid nodes as described by Eqs. (13a–13c). Of course, actual blade deflections would be much smaller; the large amplitude grid motion is shown here for clarity.

Having defined the grid motion, the unsteady variational principle, Eq. (23), is now discretized using conventional finite element techniques. In the present work, a four-node isoparametric element is used. Consider the nth element in the computational domain. The values of the unsteady velocity perturbation at the corners of the element $\{\phi\}_n$ are interpolated into the interior of the element using an interpolation of the form

$$\phi(\xi, \eta) = [N]_n \{\phi\}_n \tag{26}$$

where $[N]_n$ is a row vector of interpolation functions. The local stiffness matrix is then given by

$$[k]_n = \int\int_{D_n} \left\{ -[N']_n^T [N]_n + \frac{1}{C^2} \left[[N']_n^T \nabla' \Phi \nabla' \Phi^T [N']_n + j\omega([N']_n^T \nabla' \Phi [N]_n - [N]_n^T \nabla' \Phi^T [N']_n) + \omega^2 [N]_n^T [N]_n \right] \right\} d\xi\, d\eta \tag{27}$$

where

$$[N']_n = \begin{bmatrix} \frac{\partial N_1}{\partial \xi} & \frac{\partial N_2}{\partial \xi} & \frac{\partial N_3}{\partial \xi} & \frac{\partial N_4}{\partial \xi} \\ \frac{\partial N_1}{\partial \eta} & \frac{\partial N_2}{\partial \eta} & \frac{\partial N_3}{\partial \eta} & \frac{\partial N_4}{\partial \eta} \end{bmatrix}_n$$

The "force vector" associated with this element is given by

$$\{b\}_n^T = -\int\int_{D_n} \left\{ j\omega f^T \left(I - \frac{1}{C^2} \nabla' \Phi \nabla' \Phi^T \right) [N']_n - \frac{\omega^2}{C^2} f \cdot \nabla' \Phi [N]_n - \left(\nabla' \Phi^T \tilde{J} + \nabla' \cdot f \nabla' \Phi^T - \frac{1}{2C^2} \nabla' \Phi^T \tilde{J} \nabla' \Phi \nabla' \Phi^T \right) [N']_n + j\omega \left[\nabla' \cdot f - \frac{1}{2C^2} \nabla' \Phi^T \tilde{J} \nabla' \Phi \right] [N]_n \right\} R\, d\xi\, d\eta \tag{28}$$

The local stiffness matrix, Eq. (27), is identical to that found by Whitehead using a Galerkin method [compare with Eq. (25) of Ref. 3]. The force vector, Eq. (28), however, contains some additional terms associated with the dilation and shearing of the grid (those terms in which $\nabla' \cdot f$ and $\tilde{J}$ appear).

The local stiffness matrices and force vectors having been computed, they are then assembled into a global stiffness matrix and force vector. Also included in the global stiffness matrix are the contributions of the boundary integral terms in Eq. (23). The assembly process is simplified because of the regular structure afforded by the H grid. If the grid contains M nodes in the streamwise direction and N nodes in the circumferential direction, then there will be $M \cdot N$ nodal values of ϕ. In addition, there will be M_p Lagrange multipliers, one for each pair of periodic node points along the upstream boundary, and M_w wake displacement degrees of freedom r. To provide wake closure, $M_w - 1$ auxiliary equations are applied along the wake to enforce pressure continuity, plus one equation to specify that the wake remains attached to the trailing edge.

For unsteady flow computations, nonreflecting boundary conditions are required at the far-field boundaries so that the flowfield may be computed on a computational domain of finite extent. Without nonreflecting boundary conditions, outgoing waves would produce spurious reflections at the far-field boundary that would corrupt the solution. Previous investigators have found the exact analytical behavior of the linearized potential[1,3] and linearized Euler[5] equations and matched these analytical solutions to numerical solutions at the far-field boundary. In this paper, the exact far-field behavior of the *discretized* small disturbance equations is found by performing an eigenanalysis of the discretized equations in the far field.[10] The resulting eigenmodes are then used to construct perfectly nonreflecting boundary conditions.

The implementation of the far-field boundary conditions completes the discretization of the linearized potential equations. Because an H grid is used, the resulting matrix is block tridiagonal and may by solved efficiently using an LU decomposition algorithm that takes advantage of the block-tridiagonal structure. In the next section, some typical results of the present analysis are presented.

IV. Results

To test the present approach, a series of flat plate cascade cases were analyzed using the present method and compared with a semianalytical code (LINSUB) developed by Whitehead.[16] The cascade considered here has a gap-to-chord ratio G of 1.0, a stagger angle Θ of 45 deg, and a mean flow Mach number M of 0.7. Figure 3 shows the computed real and imaginary parts of the unsteady pressure difference across the reference airfoil for the case where the airfoils vibrate in plunge with amplitude h, reduced frequency (based on the chord) $\bar{\omega}$ of 1.0, and an interblade phase angle σ of 90 deg. These results were calculated using a 65×17 node computational grid. The agreement between the present method and Whitehead's LINSUB results is remarkably good, even in the leading-edge region where there is a square root singularity.

By integrating the unsteady pressure on the surface of the airfoil, one can compute the unsteady aerodynamic loads act-

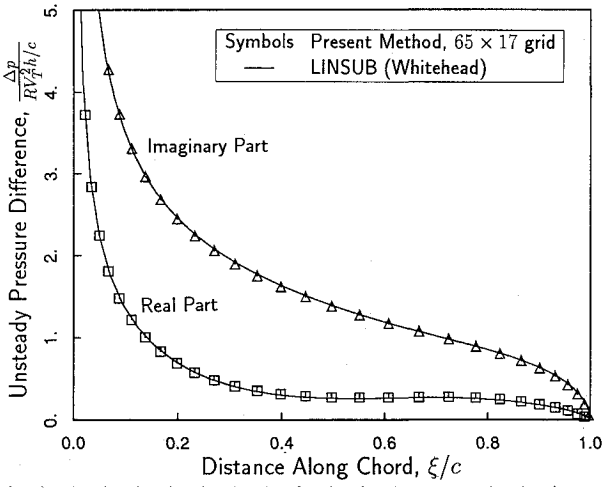

Fig. 3 Real and imaginary parts of the unsteady pressure difference across the reference airfoil of a cascade of plunging flat plate airfoils; $M = 0.7$, $G = 1.0$, $\Theta = 45$ deg, $\sigma = 90$ deg, $\bar{\omega} = 1.0$.

ing on the airfoils and, hence, determine the flutter stability of the cascade. Shown in Fig. 4 is the imaginary part of the lift for a cascade of airfoils plunging with reduced frequencies $\bar{\omega}$ of 0.5, 1.0, 1.5, and 2.0 for a range of interblade phase angles σ from -90 to $+270$ deg. These results were obtained using a 129×33 computational mesh. Also shown is the semianalytical solution calculated using Whitehead's LINSUB code. For the cases considered here, the imaginary part of the lift is negative, indicating that the motion of the airfoils is damped. The peaks in the response curves correspond to acoustic resonance. For interblade phase angles that lie between these points, the flow is said to be super-resonant. In the super-resonant region, acoustic waves propagate away from the cascade unattenuated in the duct. The overall good agreement between the present method and Whitehead's LINSUB in both the subresonant and super-resonant regions demonstrates the accuracy of the method and the effectiveness of the far-field boundary conditions. At high reduced frequencies and Mach numbers near unity, more resolution is required to accurately resolve upstream moving pressure waves. This would explain the slight degradation in solution accuracy for the highest reduced frequency in the vicinity of the acoustic resonance at an interblade phase angle of 214.5 deg.

As an example of unsteady flow through a more realistic cascade, that is, one in which the blades have finite thickness

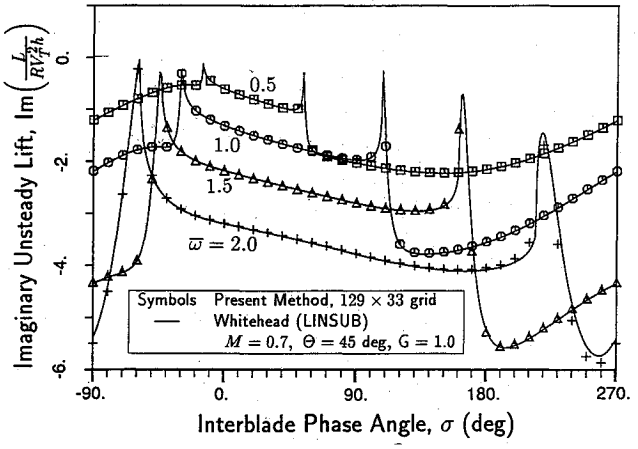

Fig. 4 Imaginary part of the unsteady lift acting on the reference airfoil of a cascade of plunging flat plate airfoils; $M = 0.7$, $G = 1.0$, $\Theta = 45$ deg.

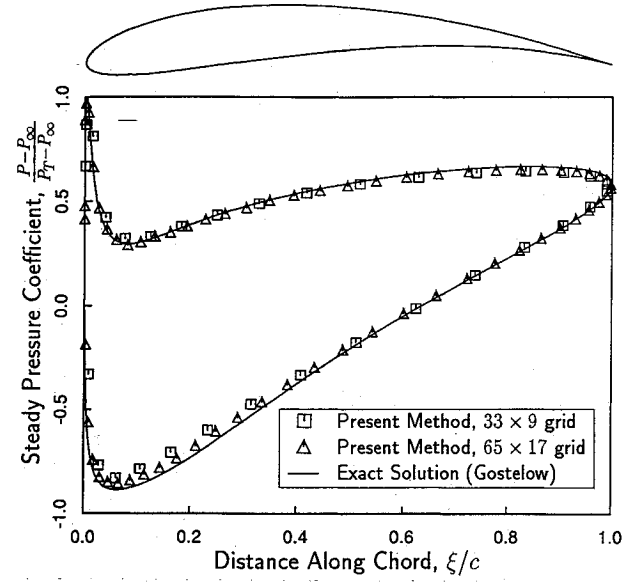

Fig. 5 Computed pressure coefficient on surface of airfoils of Gostelow cascade. The gap-to-chord ratio G is 0.9902, the stagger angle Θ is 37.5 deg, the inflow angle $\Omega_{-\infty}$ is 53.5 deg, and the upstream Mach number, $M_{-\infty}$ is 0.25.

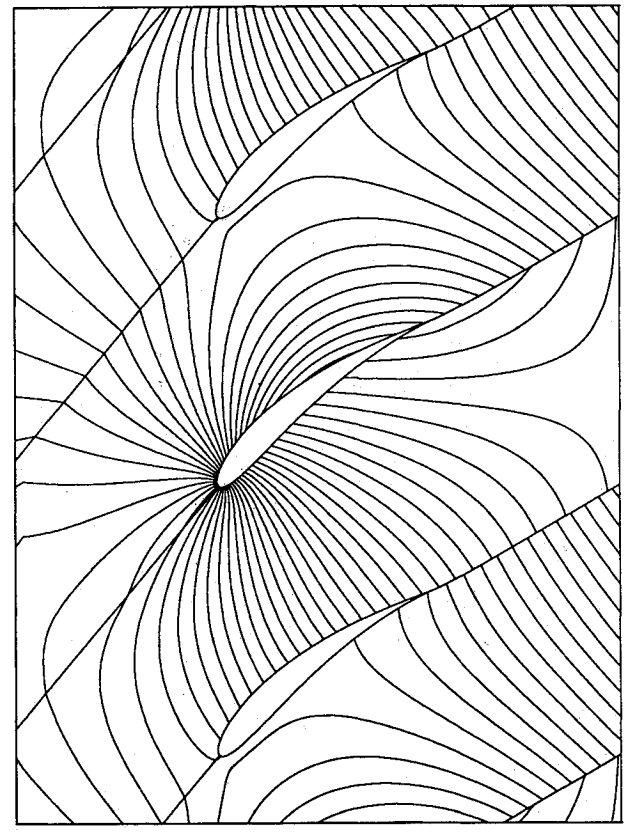

Fig. 6 Contours of unsteady perturbation potential for Gostelow airfoils pitching about their midchord. The reduced frequency $\bar{\omega}$ is 0.4, and the interblade phase angle σ is 90 deg.

and camber, we consider a cascade of Joukowski-like airfoils (see Fig. 2). The cascade has a gap-to-chord ratio G of 0.9902 and a stagger angle Θ of 37.5 deg. The inflow angle $\Omega_{-\infty}$ is 53.5 deg, and the inflow Mach number $M_{-\infty}$ is 0.25. Gostelow[17] computed the steady flow through this cascade using an exact conformal mapping technique. The steady flowfield was computed here using the present finite element technique on two different computational grids, one a 33×9 node grid and the other a 65×17 node grid. Shown in Fig. 5 is the computed steady coefficient of pressure. Also shown for comparison is the exact solution due to Gostelow. Note the generally good agreement between the finite element results and the exact theory.

Having computed the mean flowfield in the cascade, the unsteady flowfield is next found for the case where the airfoils oscillate in pitch about their midchords with a reduced frequency $\bar{\omega}$ of 0.4 and an interblade phase angle σ of 90 deg. The computed unsteady velocity potential is shown in Fig. 6 in the strained coordinate system (ξ, η). Several interesting features of the solution are clearly seen. First, the potential contours are kinked at the upstream periodic boundaries. This is because the grid velocity is only C^0 continuous across the periodic and wake boundaries. Second, because this is a subresonant case, the potential decays in the upstream far-field region. Third, the potential is seen to be discontinuous across the wake due to the unsteady shed vorticity resulting from the unsteady circulation about the airfoil. Fourth, the unsteady potential solution passes smoothly out of the computational domain without spurious reflections, demonstrating the effectiveness of the far-field boundary conditions.

Shown in Fig. 7 are the real and imaginary surface pressures for this same case. These solutions were computed on three different computational grids (a 33×9, a 65×17, and a 129×33 node grid) to assess the accuracy of the present linearized harmonic potential technique. Note that the agree-

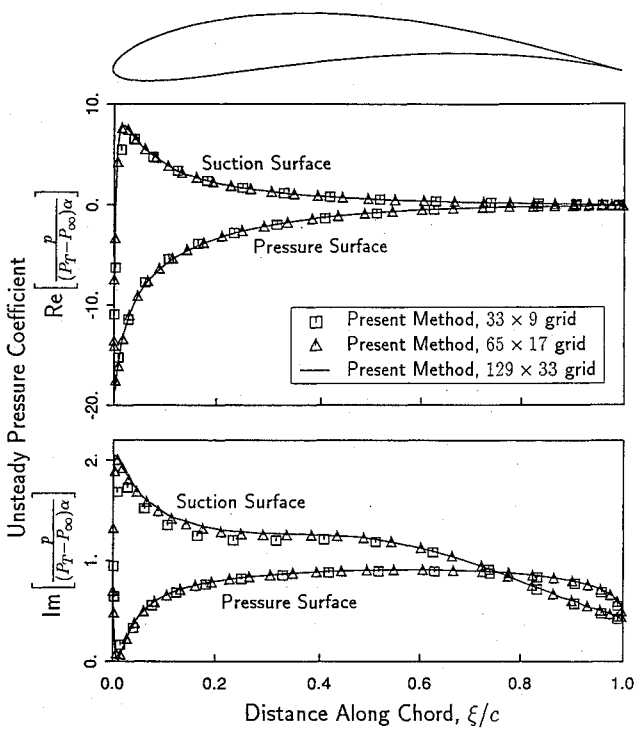

Fig. 7 Real and imaginary parts of unsteady surface pressure for cascade of Gostelow airfoils pitching about their midchord. The reduced frequency $\bar{\omega}$ is 0.4, and the interblade phase angle σ is 90 deg.

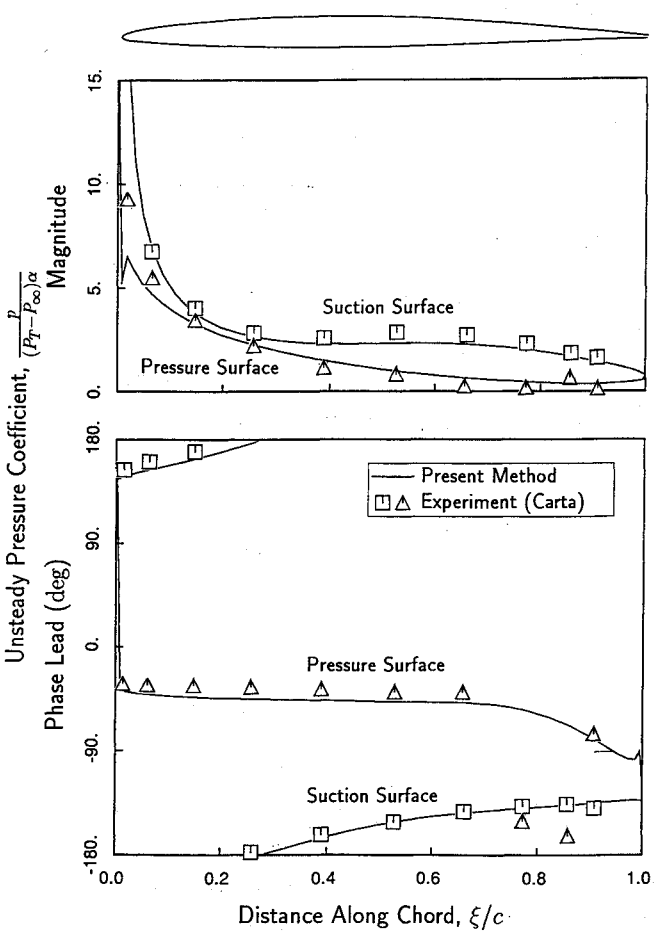

Fig. 8 Magnitude and phase of unsteady pressure on airfoil surfaces of low-speed compressor cascade; $M_{-\infty} = 0.17$, $G = 0.75$, $\Theta = 55$ deg, $\Omega_{-\infty} = 66$ deg, $\sigma = -90$ deg, and $\bar{\omega} = 0.244$ (first standard configuration, case 8).

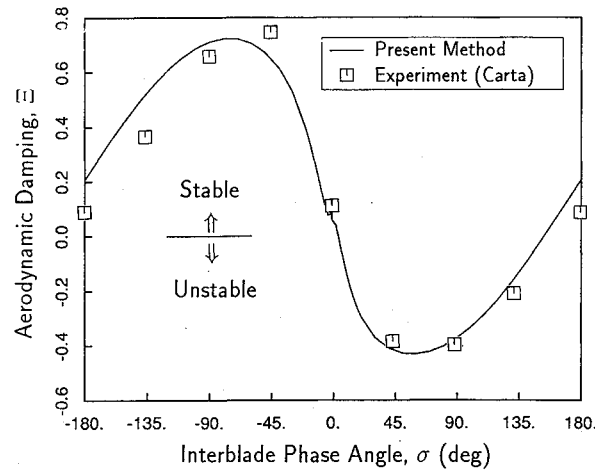

Fig. 9 Aerodynamic damping acting on pitching airfoils of low speed compressor cascade; $M_{-\infty} = 0.17$, $G = 0.75$, $\Theta = 55$ deg, $\Omega_{-\infty} = 66$ deg, and $\bar{\omega} = 0.244$ (first standard configuration).

ment among the three computed solutions is quite good, especially for the real part of the unsteady surface pressure. The largest discrepancies occur in the imaginary part near the leading edge of the suction surface. However, the differences seen among the coarse, medium, and fine grid cases are on a par with the differences seen in the steady solution for these three computational grids (see Fig. 5). Generally speaking, the present method is capable of predicting unsteady flowfields with the same level of accuracy as a comparable steady flow solver for moderate (order unity) to low reduced frequencies.

Next, consider the case of a low-speed compressor cascade. This cascade, known as the first standard configuration,[18] was studied experimentally by Carta.[19] The cascade is composed of airfoils that have 10 deg of camber and are 6% thick. The stagger angle Θ is 55 deg, and the gap-to-chord ratio G is 0.75. The reported inflow angle $\Omega_{-\infty}$ is 66 deg, and the inflow Mach number M is 0.17. For the case considered here, the airfoils vibrate in pitch about a point near their midchords with a reduced frequency $\bar{\omega}$ of 0.244 and an interblade phase angle σ of -90 deg. The computed magnitude and phase of the unsteady surface pressure are shown in Fig. 8 along with the experimental results of Carta. The computational results were obtained using a 65×17 node grid. Overall, the agreement between the present analysis and the experiment is quite good. The large discrepancy in the phase of the unsteady pressure on the pressure surface near the trailing edge is most likely due to the difficulty of experimentally measuring the phase when the magnitude is small.

Similar computations were carried out for a range of interblade phase angles, and the aerodynamic damping Ξ was computed by direct integration of the pressure distribution. Figure 9 shows the aerodynamic damping Ξ acting on the airfoils of the first standard configuration as a function of interblade phase angle σ. Negative aerodynamic damping leads to the aeroelastic instability known as flutter. This cascade is seen to be unstable in pitch for interblade phase angles between approximately 0 and 150 deg. Note also that the present method is in good agreement with the experimental results of Carta over the entire range of interblade phase angles. These results demonstrate the ability of the present finite method to predict accurately unsteady flows in lightly loaded compressor cascades.

To demonstrate the ability of the present analysis to predict accurately unsteady flows in the high subsonic flow regime, we next consider the tenth standard configuration compressor cascade.[20,21] The airfoils in this cascade have a NACA 0006 thickness distribution slightly modified so that the airfoil trailing edge is wedged rather than blunt. The camber line is a circular arc; the maximum height of the camber line is 5% of the chord. The stagger angle Θ is 45 deg, and the gap to chord

ratio G is 1.0. For the subsonic case considered here, the inflow angle $\Omega_{-\infty}$ is 55 deg, and the Mach number $M_{-\infty}$ is 0.7. Shown in Fig. 10 is the computed steady Mach number. Note that the maximum Mach number on the suction surface is about 0.92. These solutions were obtained using three different grid resolutions (33 × 9, 65 × 17, and 129 × 33 nodes). The agreement among the three solutions is quite good, even between the coarse and fine grid solutions. The largest discrepancy is on the suction surface at about the 25% chord point.

Next, we consider the case of the airfoils vibrating in pitch about their midchords with a reduced frequency $\bar{\omega}$ of 1.0 and an interblade phase angle σ of 180 deg. The unsteady pressure

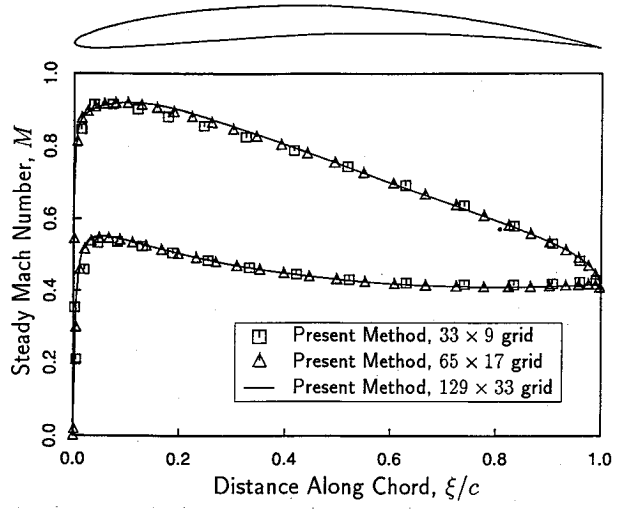

Fig. 10 Steady Mach number distribution on airfoil surfaces of the tenth standard configuration cascade; $M_{-\infty}=0.70$, $G=1.0$, $\Theta=45$ deg, and $\Omega_{-\infty}=55$ deg.

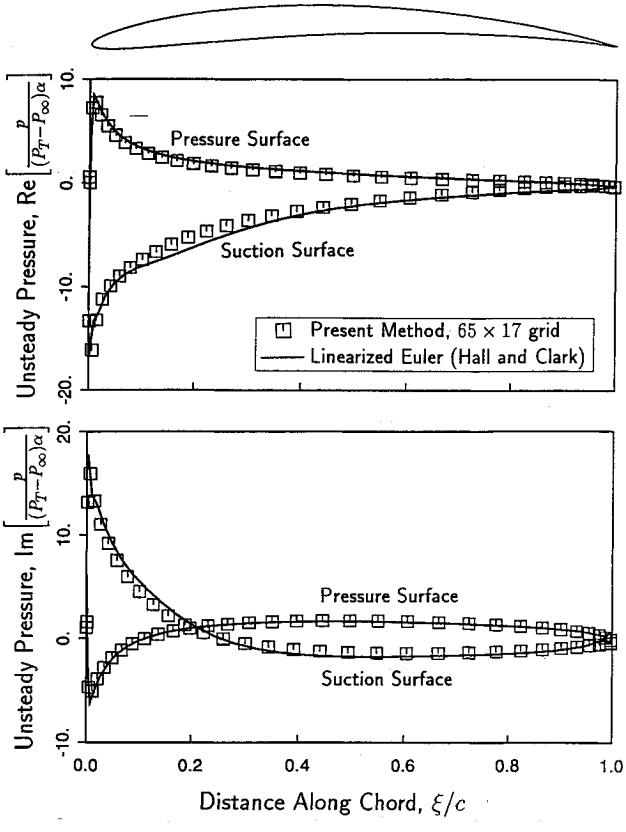

Fig. 11 Real and imaginary parts of unsteady surface pressure for airfoils vibrating in pitch; $M_{-\infty}=0.70$, $G=1.0$, $\Theta=45$ deg, $\Omega_{-\infty}=55$ deg, $\bar{\omega}=1.0$, and $\sigma=180$ deg (tenth standard configuration).

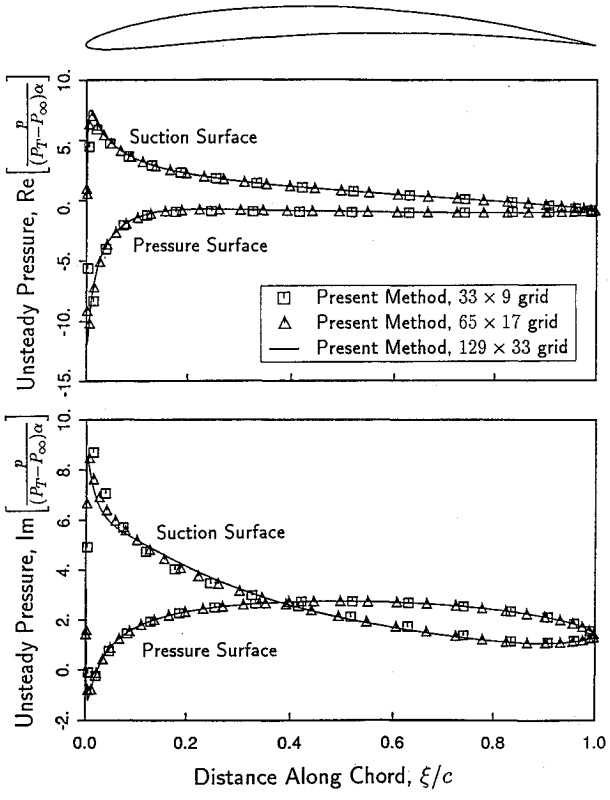

Fig. 12 Real and imaginary parts of unsteady surface pressure for airfoils vibrating in pitch; $M_{-\infty}=0.70$, $G=1.0$, $\Theta=45$ deg, $\Omega_{-\infty}=55$ deg, $\bar{\omega}=1.0$, $\sigma=90$ deg (tenth standard configuration, case 8).

distribution on the surface of the reference airfoil is shown in Fig. 11. Also shown is the unsteady pressure distribution calculated using a linearized Euler solver developed by Hall and Clark.[10,11] The agreement between these two solution techniques is very good, with only minor discrepancies in the computed pressures on the suction surface near the leading edge.

The last case presented is similar to the preceding example. Again, the airfoils vibrate in pitch with a reduced frequency $\bar{\omega}$ of 1.0, but the interblade phase angle σ is now 90 deg. Shown in Fig. 12 is the pressure distribution on the reference airfoil as computed using three grids with different resolutions. Again, the three solutions are in good agreement with one another, and the accuracy of the unsteady solutions is on a par with the accuracy of the steady solutions (see Fig. 10). Also, note that the solutions are well behaved in the vicinity of the leading and trailing edges, even the solution obtained on the coarse 33 × 9 node grid. This good behavior is attributed to the use of a deforming computational mesh. Solutions of this accuracy would be difficult to obtain using a computational grid fixed in space due to errors introduced by extrapolation terms required at the airfoil boundary.

Finally, it should be mentioned that the present unsteady analysis is extremely efficient. For the preceding case, for example, the steady solution on the 65 × 17 node grid required about 8.7 s of computer time to converge on a Stardent 3000 workstation. The unsteady solution procedure—including the generation of the moving grid and the eigenanalysis of the far field—required just 8.9 s. Hence, the unsteady code requires about the same amount of computer time as the steady code.

V. Concluding Remarks

In this paper a finite element method for calculating unsteady small disturbance flows in subsonic cascades is presented. The method is based on a linearized version of Bateman's variational principle that describes the unsteady small disturbance flow about a fully nonlinear mean flow. The

description of the unsteady flowfield by a variational principle has a number of advantages. For example, the effects of the vibrating blades and deforming computational grid are automatically taken into account. In fact, the natural boundary conditions on the airfoil surface are found to be the desired upwash boundary conditions. Furthermore, the variational principle is easily discretized using standard finite element techniques. Unfortunately, no such variational principle exists for the Euler or Navier-Stokes equations.

The use of a deforming grid that conforms to the instantaneous position of the airfoil eliminates extrapolation terms that are a significant source of error in fixed-grid calculations. The linearized potential solver is both fast and accurate and, therefore, is a useful tool for the analysis of unsteady flow in turbomachinery. Numerical experiments have demonstrated that for low-to-moderate reduced frequencies, the numerical accuracy of the linearized potential method is on a par with steady flow solvers and that engineering accuracy results can be obtained with fairly coarse grids.

References

[1]Verdon, J. M., and Caspar, J. R., "Development of a Linear Unsteady Aerodynamic Analysis for Finite-Deflection Subsonic Cascades," *AIAA Journal,* Vol. 20, No. 9, 1982, pp. 1259–1267.

[2]Verdon, J. M., and Caspar, J. R., "A Linearized Unsteady Aerodynamic Analysis for Transonic Cascades," *Journal of Fluid Mechanics,* Vol. 149, Dec. 1984, pp. 403–429.

[3]Whitehead, D. S., "A Finite Element Solution of Unsteady Two-Dimensional Flow in Cascades," *International Journal for Numerical Methods in Fluids,* Vol. 10, No. 1, Jan. 1990, pp. 13–34.

[4]Ni, R. H., and Sisto, F., "Numerical Computation of Nonstationary Aerodynamics of Flat Plate Cascades in Compressible Flow," *Transactions of the ASME: Journal of Engineering for Power,* Vol. 98, No. 2, April 1976, pp. 165–170.

[5]Hall, K. C., and Crawley, E. F., "Calculation of Unsteady Flows in Turbomachinery Using the Linearized Euler Equations," *AIAA Journal,* Vol. 27, No. 6, 1989, pp. 777–787.

[6]Rausch, R. D., Batina, J. T., and Yang, H. T. Y., "Euler Flutter Analysis of Airfoils Using Unstructured Dynamic Meshes," *Proceedings of the AIAA/ASME/ASCE/AHS/ASC 30th Structures, Structural Dynamics and Materials Conference* (Mobile, AL), AIAA, Washington, DC, April 1989, (AIAA Paper 89-1384).

[7]Venkatakrishman, V., and Jameson, A., "Computation of Unsteady Transonic Flows by the Solution of Euler Equations," *AIAA Journal,* Vol. 26, No. 8, 1988, pp. 974–981.

[8]Huff, D. L., and Reddy, T. S. R., "Numerical Analysis of Supersonic Flow Through Oscillating Cascade Sections by Using a Deforming Grid," AIAA Paper 89-2805, July 1989.

[9]Huff, D. L., Swafford, T. W., and Reddy, T. S. R., "Euler Flow Predictions for an Oscillating Cascade Using a High Resolution Wave-Split Scheme," ASME Paper 91-GT-198, 36th International Gas Turbine and Aeroengine Congress and Exposition, Orlando, FL, June 3–6, 1991.

[10]Hall, K. C., and Clark, W. S., "Prediction of the Forced Response of Turbomachinery Blading Using the Linearized Harmonic Euler Equations on Deforming Grids," *AIAA Journal,* Vol. 31, No. 3, 1993, pp. 540–550.

[11]Hall, K. C., and Clark, W. S., "Calculation of Unsteady Linearized Euler Flows in Cascades Using Harmonically Deforming Grids," *Unsteady Aerodynamics, Aeroacoustics, and Aeroelasticity of Turbomachines,* edited by H. M. Atassi, Springer-Verlag, New York, 1993, pp. 195–212.

[12]Holmes, D. G., and Chuang, H. A., "2D Linearized Harmonic Euler Flow Analysis for Flutter and Forced Response," *Unsteady Aerodynamics, Aeroacoustics, and Aeroelasticity of Turbomachines,* edited by H. M. Atassi, Springer-Verlag, New York, 1993, pp. 213–230.

[13]Bateman, H., "Irrotational Motion of a Compressible Fluid," *Proceedings of the National Academy of Sciences,* Vol. 16, No. 12, Dec. 15, 1930, p. 816–825.

[14]Lighthill, M. J., "A Technique for Rendering Approximate Solutions to Physical Problems Uniformly Valid," *Philosophical Magazine,* Ser. 7, Vol. 40, No. 311, Dec. 1949, pp. 1179–1201.

[15]Thompson, J. F., Thames, F. C., and Mastin, W., "A Code for Numerical Generation of Boundary-Fitted Curvilinear Coordinate Systems on Fields Containing any Number of Arbitrary Two-Dimensional Bodies," *Journal of Computational Physics,* Vol. 24, No. 3, 1977, pp. 274–302.

[16]Whitehead, D. S., "Classical Two-Dimensional Methods," *AGARD Manual on Aeroelasticity in Axial-Flow Turbomachines, Unsteady Turbomachinery Aerodynamics,* Vol. 1, edited by M. F. Platzer and F. O. Carta, AGARD-AG-298, March 1987, Chap. II.

[17]Gostelow, J. P., *Cascade Aerodynamics,* Pergamon, Oxford, England, UK, 1984, pp. 86–108.

[18]Bölcs, A., and Fransson, T. H., "Aeroelasticity in Turbomachines Comparison of Theoretical and Experimental Cascade Results," Air Force Office of Scientific Research, AFOSR-TR-87-0605, Washington, DC, 1986.

[19]Carta, F. O., "Unsteady Gapwise Periodicity of Oscillating Cascaded Airfoils," American Society of Mechanical Engineers, ASME Paper 82-GT-286, New York, April 1982.

[20]Verdon, J. M., and Usab, W. J., Jr., "Advances in the Numerical Analysis of Linearized Unsteady Cascade Flows," Air Force Wright Aeronautical Laboratories Rept. AFWAL-TR-88-2055, Wright-Patterson AFB, OH, Aug. 1988.

[21]Fransson, T. H., private communication, June 1991.